Complete title: Three-dimensional visualization of moss rhizoid system by refraction-contrast X-ray micro-computed tomography

Running title

X-ray micro-CT of moss rhizoid system

Authors:

Ryohei Yamaura [1], Daisuke Tamaoki[2], Hiroyuki Kamachi[2], Daisuke Yamauchi[3], Yoshinobu Mineyuki[3], Kentaro Uesugi[4], Masato Hoshino[4], Tomomi Suzuki [5], Toru Shimazu[6], Haruo Kasahara[7], Motoshi Kamada[8], Yuko T. Hanba[9], Atsushi Kume[10], Tomomichi Fujita[11], *Ichirou Karahara[2]

Address:

[1]Department of Biology, Graduate School of Science and Engineering for Education, University of Toyama, 3190 Gofuku, Toyama 930-8555, Japan, [2]Faculty of Science, University of Toyama, 3190 Gofuku, Toyama 930-8555, Japan, [3]Graduate School of Science, University of Hyogo, 2167 Shosha, Himeji, Hyogo 671-2280, Japan, [4]Japan Synchrotron Radiation Research Institute, 1-1-1 Kouto, Sayo, Sayo-gun, Hyogo 679-5198, Japan, [5]Kibo Utilization Center, Human Spaceflight Technology Directorate, Japan Aerospace Exploration Agency, 2-1-1 Sengen, Tsukuba 305-8505, Japan, [6]Technology and Research Promotion Department, Japan Space Forum, 3-2-1 Kandasurugadai, Tokyo 101-0062, Japan, [7]ISS Utilization and Operations Department, Japan Manned Space Systems Corp., 1-1-26 Kawaguchi, Tsuchiura 300-0033, Japan, [8]Future Development Division, Advanced Engineering Services Co., Ltd., 1-6-1 Takezono, Tsukuba, Ibaraki 305-0032, Japan, 1-1-26 Kawaguchi, Tsuchiura 300-0033, Japan, [9]Faculty of Applied Biology, Kyoto Institute of

Technology, Matsugasaki, Sakyo-ku, Kyoto 606-8585, Japan, [10]Faculty of Agriculture, Kyushu University, 744 Motooka, Nishi-ku, Fukuoka 819-0395, Japan [11]Faculty of Science, Hokkaido University, Kita 10 Nishi8 Kita-ku, Sapporo, Hokkaido 060-0810, Japan

*To whom correspondence should be addressed.

E-mail: karahara@sci.u-toyama.ac.jp

Ichirou Karahara

Department of Biology, Faculty of Science, University of Toyama, 3190 Gofuku, Toyama 930-8555, Japan

Tel: + 81-76-445-6630 Fax: + 81-76-445-6549

Keywords: *Physcomitrium* (*Physcomitrella*), rhizoid system, SPring-8, 3D architecture, X-ray micro-CT, synchrotron radiation

The total number of pages:

The total number of figures: 9

The total number of tables: 1

The total number of supplementary figures: 2

Abstract

Land plants have two types of shoot-supporting systems, root system and rhizoid system, in vascular plants and bryophytes. However, since the evolutionary origin of the systems are different, how much they exploit common systems or distinct systems to architect their structures are largely unknown. To understand the regulatory mechanism how bryophytes architect rhizoid system responding to an environmental factor, such as gravity, and compare it with the root system of vascular plants, we have developed the methodology to visualize and quantitatively analyze the rhizoid system of the moss, *Physcomitrium patens* in 3D. The rhizoids having the diameter of 21.3 μm on the average were visualized by refraction-contrast X-ray micro-CT using coherent X-ray optics available at synchrotron radiation facility SPring-8. Three types of shape (ring-shape, line, black circle) observed in tomographic slices of specimens embedded in paraffin were confirmed to be the rhizoids by optical and electron microscopy. Comprehensive automatic segmentation of the rhizoids which appeared in different three form types in tomograms was tested by a method using Canny edge detector or machine learning. Accuracy of output images was evaluated by comparing with the manually-segmented ground truth images using measures such as F1 score and IoU, revealing that the automatic segmentation using the machine learning was more effective than that using Canny edge detector. Thus, machine learning-based skeletonized 3D model revealed quite dense distribution of rhizoids, which was similar to root system architecture in vascular plants. We successfully visualized the moss rhizoid system in 3D for the first time.

(250 words)

Main text

Introduction

Rooting structure of vascular plants is called the root systems consisting of individual roots.

The root system provides a basis for supporting and anchoring the upper part of the plants for growth by uptaking water and minerals from substrate, such as soil. The root system adapts itself to surrounding soil environment changing its architecture [1]. Understanding how the plant root system adapts themselves flexibly to the surrounding environment is important for optimization of plant cultivation conditions under given environment.

An individual rhizoid of mosses is a multi-cellular filament [2], and its morphology is totally different from an individual root of vascular plants, which is an organ composed of multiple tissues. Nevertheless, the rhizoids of the Bryophyte, the first land plants, has functions of supporting and anchoring the upper part of the plants as well as uptaking water and minerals from soil, similarly to the roots of vascular plants. Therefore, whole rhizoids, which belong to one individual gametophore, with their architectural organization called "the rhizoid system" hereafter for convenience, which is commonly used in previous literatures as contrasted with the root system of the vascular plants [3].

One of the most important environmental factors that affect architecture of the rooting structures is gravity. And the rhizoids of mosses show positive gravitropism in darkness [4]. Considering these common functional characteristics, therefore, understanding the regulatory mechanism of organizing the rhizoid system and comparing it with that of the root system of vascular plants would give a clue to understand how land plants evolved this mechanism.

In order to understand adaptive mechanisms of the root and rhizoid systems to different environmental factors, it is necessary to visualize their morphology in 3D and to extract quantitative parameters describing its 3D morphology. Exploring the methodology of 3D morphological analysis of compact rhizoid system will provide a model system that facilitates to analyze that of the root system architecture of vascular plants as well. Hypergravity experiments have been performed using centrifuges to investigate effects of

gravity on various physiological phenomena [5, 6], where it has already been reported that length of the rhizoids and a whole mass (dry weight) of the rhizoid system of a model moss, *Physcomitrium* (*Physcomitrella*) *patens* increased under hypergravity. Investigating responses of moss rhizoid system to altered gravitational conditions will lead to understand the mechanism of architectural regulation in mosses and in root system of vascular plants by gravity.

With the aim to understand adaptive mechanisms of the root system of vascular plants to environmental factors, X-ray micro-CT is developed. Industrial CT scanners or a scanning system employing microfocus X-ray source has been widely used to visualize roots of crop plants [7-13]. On the other hand, we have reported that refraction-contrast X-ray micro-CT using coherent X-ray optics enabled to visualize thin dried secondary roots of a model plant Arabidopsis having the thickness of its isosurface model at 20.9 μm on the average [14]. Such a higher spatial resolution imaging method can be applicable to visualize thin rhizoids of mosses.

Recently, we have performed "Space Moss" experiment on the International Space Station to understand effects of microgravity on the growth of *P. patens* [15]. In the present study, we have at first aimed to visualize its rhizoid system architecture in 3D by refraction-contrast X-ray micro-CT using specimens obtained by the Space Moss experiment. We also investigated the rhizoid system architecture under a hypergravity condition performed on the ground to examine effects of altered gravitational conditions. While we have manually traced the signal of the root in the obtained tomograms and made 3D models in the previous study [14], here we undertook automatic segmentation methods of the rhizoid area based on image processing techniques such as contour extraction as well as that based on machine learning. Images obtained by automatic segmentation was compared with the ground truth images obtained by manual segmentation and confusion matrices were formed. Accuracy of

automatic segmentation was evaluated by comparing indicators such as F1 score and IoU, revealing that the automatic segmentation based on machine learning was more effective than that using contour extraction. Isosurface and skeletonized models of the rhizoid system were visualized in 3D for the first time. Three-dimensional visualization and digitalization of complex network of the rhizoid system will be also applicable to visualize such as 3D distribution of root hairs of vascular plants and hyphal architecture of mycorrhizal fungi interacting with roots, which will give insight into how architecture of rooting system of land plants is evolved under the Earth's environment.

Methods and materials

Plant materials and growth conditions

Plant materials used in the present study was *Physcomitrium* (*Physcomitrella*) *patens* (Hedw.) Bruch et Schimp. These were obtained by the Space Moss experiment which was performed from 2019 to 2020 (Run 1, 2, and 3) as well as by the hypergravity experiment performed on the ground. Growth conditions of the Space Moss experiment are as follows. Forty-eight gametophores were planted on the ground on an agar slab (W × D × H = 54 × 44 × 25 mm) containing BCD medium [16] in a polycarbonate growth chamber having the outer dimensions of W × D × H = 60 × 50 × 60 mm. Growth chambers were installed in the Plant Experimental Units (PEU), which was designed for experiments in the International Space Station [17]. Plants were kept refrigerated until the start of the experiment. PEUs were installed either in a microgravity compartment or on a centrifuge of to produce artificial gravity in the CBEF [18, 19] in the ISS. This artificial 1 × *g* condition is referred to as Space 1 × *g*. For the ground control experiments, PEUs were installed in the Cell Biology Experimental Facility (CBEF) at Tsukuba Space Center. Plants were illuminated from the top with LED matrix [19] with the light intensity of 30 μmol m^{-2} s^{-1} at the bottom center of the

growth chamber. Plants were grown for 25-26 days at 25 ˚C. Run 1 and 2 experiments were performed from Jul. to Aug., 2019 and from Dec. 2020 to Jan., 2021, respectively. For the record, specimens of Space Moss experiment used in the present study were as follows: Ground 1 × *g*_SN17; Ground 1 × *g*_27, 82; Space 1 × *g*_005; Space 1 × *g*_003, B003, 004; Space μ × *g*_102.

Growth conditions of the hypergravity experiment were basically the same as described previously [5] using MK3 centrifuge (Matsukura Co., Toyama, Japan) with the ground control experiments. Plants were grown under 10 × *g* or 1 × *g* (as the control) for 25-26 days at 25 ˚C. For the record, specimens of hypergravity experiment used in the present study were as follows: Ground 1 × *g*_3; Ground 10 × *g*_1, 2.

Chemical fixation and embedding of rhizoid system specimens

The moss plants cultivated on orbit (Run 1 and 2 experiments) were chemically fixed on orbit together with the agar medium in 100 mM sodium-phosphate buffer (pH 7.2) containing 2.5 % (v/v) glutaraldehyde (Polysciences, Inc., Warrington, USA), and were kept refrigerated until the start of embedding process on the ground (Fig. 1a). Specimens were embedded in paraffin primarily for X-ray micro-CT and optical microscopy while those were embedded in LR White resin primarily for electron microscopy.

For specimen embedding in paraffin, fixed plant specimens of Run 1 were dehydrated in a graded ethanol series (70, 90, 99.9, 100 % (v/v)) and xylene in glass vials, which were placed on a rotary shaker (80 rpm). Specimens were then infiltrated with paraffin (Paraplast plus, Sigma-Aldrich Japan, Tokyo, Japan) for 3 days at 60 ˚C.

For specimen embedding in LR White resin (Electron Microscopy Sciences, Hatfield, USA), plant specimens of Run 2 chemically-fixed on orbit as mentioned above and plant specimens of hypergravity experiment (10 × *g* or 1 × *g* as the control) were fixed or

170 refixed in 50 mM sodium-cacodylate buffer (pH 7.2) containing 2.0 % (v/v) glutaraldehyde
171 and 1.0 % (w/v) paraformaldehyde (Wako Pure Chemicals, Osaka, Japan) at 4 ˚C for 12 h.
172 The specimens were washed with DDW and were post-fixed at 4 ˚C for 3 h with 50 mM
173 sodium-cacodylate buffer (pH 7.2) containing 1 % (w/v) osmium tetroxide. The fixed
174 specimens were dehydrated in a graded ethanol series and were embedded in LR White resin.
175 The fixed specimens were stained *en bloc* with EM stainer (Nisshin EM, Tokyo, Japan)
176 during dehydration at the step of 10 % (v/v) ethanol.
177
178 **Optical microscopy of paraffin sections**
179 Sections of 15 μm in thickness were cut using a rotary microtome from the specimens
180 embedded in paraffin (Fig. 1b) and remained specimens were observed by X-ray micro-CT.
181 Paraffin sections were mounted on slide glasses with gelatin adhesive, were extended at 40 ˚C
182 on a hotplate, and were deparaffinized with graded xylene and ethanol series. Deparaffinized
183 sections were stained with aqueous solution of 0.05 % (w/v) Toluidine blue O. Digital
184 photographs were taken using a digital camera Cool Snap cf (Nippon Roper KK, Tokyo,
185 Japan) or DS-Ri1 (Nikon, Tokyo, Japan) fitted to an optical microscope (BX-50, Olympus
186 Corp., Tokyo, Japan).
187
188 **Electron microscopy of ultrathin sections**
189 Ultrathin sections of 80 nm in thickness were cut using an ultramicrotome (EM UC7, Leica
190 Microsystems GmbH, Wetzlar, Germany) from the specimens embedded in LR White resin,
191 were stained with lead citrate for 1.5 min, and were observed under a transmission electron
192 microscope (H-7650, Hitachi High-Tech Corp., Tokyo, Japan) at 80 kV.
193
194 **Refraction contrast X-ray micro-CT and tomographic reconstruction**

195 Refraction contrast X-ray micro-CT was performed at the experimental Hutch 1 of the
196 beamline BL20B2 of the SPring-8 synchrotron radiation facility at Japan Synchrotron
197 Radiation Research Institute, according basically to the method described previously [14, 20].
198 Its experimental setup is shown in Fig. 1c and a brief overview of the method is as follows.
199 The X-ray energy was adjusted to 15 keV. The images consecutively projected on the
200 fluorescent screen were recorded by a CMOS camera (ORCA-Flash 4.0, Hamamatsu
201 Photonics KK, Hamamatsu, Japan). Size of the obtained images was 2048 × 2048 pixels (ca.
202 5 × 5 mm). A series of 900 projections were recorded over 180 degrees. Because the rhizoids
203 distributed deeper than 5 mm from the base of the gametophore, observation was separately
204 done for the areas from the base to 5 mm below and from 5 mm to 10 mm below. The spatial
205 (pixel) resolution of the 3-D structure was estimated to be 2.71 or 2.75 μm $pixel^{-1}$. The
206 convolution back projection method was used for tomographic reconstruction. Chesler filter,
207 which is provided by the software package SP-μCT (http://www-bl20.spring8.or.jp/xct/), was
208 used for reconstruction as previously determined [14]. Tomographic slices were obtained and
209 3-D models (isosurface, wireframe) were drawn using the IMOD software package [21] as
210 previously described [22].
211 For comparing tomographic images with electron microscopic images, tomographic
212 images had to be obtained particularly at the edge surface of a specimen just beneath where
213 ultrathin sections were cut. However, structures near the edge surface of the specimen were
214 hardly visible due to an artifact. To avoid this artifact, the edge surface of the specimen was
215 covered with paraffin before scanning.
216
217 **Automatic segmentation of rhizoid area**
218 Two methods were applied for automatic segmentation of cross-sectional areas of rhizoids
219 (Fig. 2). One is based on contour extraction using Canny's edge detection algorithm [23].

Contrast of the volume was normalized and equalized using Enhance Contrast function of Fiji software package (https://imagej.net/software/fiji/) [24] with saturated pixels at 0.3 %. Canny Edge Detector plugin of Fiji [25] was applied for each tomographic slice and contours were extracted from where intensity gradient is high with the following settings: Gaussian kernel radius at 2, Low threshold at 2.5, High threshold at 6. Then Closing (3D) plugin which connects interrupted rhizoid contours with the setting of Element Shape as Cube (X, Y, and Z radii are 1, 1, and 1, respectively) and Fill holes (3D) plugin which remove holes inside particles were applied. Both of them are MorphoLibJ (Release 1.5.0) plugins of Fiji [26].

The other uses Trainable Weka Segmentation 3D (TWS 3D) plugin of Fiji software, which is based on pixel-based segmentation algorithms using machine learning [27]. In this program, pixels annotated manually by users are learned and a classifier is built by the machine learning platform WEKA (Waikato Environment for Knowledge Analysis) [28]. Mean and Variance filters, which extract features of the input images, and Fast Random Forest classifier were used as the default settings. A reconstructed volume was divided into substacks, each of which is composed of 100 transverse tomograms. In a representative substack, rhizoids and background pixels were manually annotated as independent classes in a part of a tomogram using Freehand selections tool and saved as a classifier model to train the classifier. This training was repeated for several times and the trained classifier was used to obtain a prediction result (Fig. 2b).

Evaluation of the automatic segmentation methods

Automatically-segmented rhizoid areas by the two methods mentioned above were compared with manually-segmented areas to evaluate the results as follows. As examples, 9 different areas of 256 × 256 pixels sampled from 4 tomograms of the specimens of Ground 1 × *g*_27, Ground 1 × *g*_82, Space 1 × *g*_004, and Space μ × *g*_102. Rhizoid areas obtained by

automatic segmentation were compared with those done by manual segmentation (ground truth). Pixels in an image were categorized into either of the following four groups, true positive (TP), false positive (fp), false negative (fn), or true negative (tn) (Supplementary Fig. 2), where a pixel in the rhizoid area is positive and that in the background area is negative in the ground truth image.

Calculations for the evaluation were performed using a program written in Python as follows. Automatically and manually-segmented images were transformed to matrices, where each pixel of the rhizoid and background areas in the images was assigned to values '1' or '0', respectively. In the resulting matrix which was obtained by a subtraction of an automatically-segmented image matrix from its corresponding manually-segmented image matrix (MS), an element as value '1' or '-1' was judged as fn or fp, respectively. Matrices showing distribution of fn and fp were designated as FN and FP, respectively. A matrix showing distribution of tp, TP, was obtained by a subtraction of FN from MS. A matrix showing distribution of tn, TN, was obtained by subtracting the FN, FP, TP from MS. A confusion matrix was constructed by counting the number of elements in each matrix. Accuracy, F1 score which indicates how accurately rhizoid areas are labeled, and Intersection over Union (IoU) which indicates how similar predicted rhizoid area is to the ground truth were calculated using formulas shown in Supplementary Fig. 2e.

Skeletonization of automatically-segmented rhizoid area

An isosurface model was made from a part of an image stack file obtained by automatic segmentation of rhizoid areas using 'imod auto' command in the IMOD software package. Skeletonization of the isosurface models of the rhizoids was done using Skeletonize (2D/3D) plugins of Fiji software.

Results

Observation of specimens embedded in paraffin by X-ray micro-CT

On the overview of a cross-sectional tomogram many structures can be seen (Fig. 3a). These structures are considered to be rhizoids, which needed to be verified. When a closer look was taken at a cross sectional tomogram of the rhizoid system embedded in paraffin, three types of filamentous structures were observed (Fig. 3b-d). The first one, which is referred to as Type A structure, appeared ring-shaped (Fig. 3b). The second one, which is referred to as Type B structure, appeared linear (Fig. 3c). The 3rd one, which is referred to as Type C structure, is a void space appeared as a black circle with a halo (Fig. 3d). However, in some cases, even one filamentous structure appeared in different forms from Type A thorough Type C depending on the location when viewed in 3D (Supplementary Fig. 1). From this observation, we inferred that these types of filamentous structures are different forms of rhizoids.

Comparison of tomograms and optical microscopic images of the three types of the filamentous structure

To test this hypothesis and to understand why rhizoids take such different forms, tomographic images and their corresponding optical microscopic images of the three types of the filamentous structures were compared. For this test, paraffin-embedded specimens of the hypergravity experiment performed on the ground were used instead to save the entire forms of irreplaceable specimens of Space Moss experiment. After reconstructing volumes by X-ray micro-CT, the three types of filamentous structures were observed on cross-sectional tomograms. Then actual cross-sections were cut from the paraffin-embedded specimens using a microtome at the corresponding positions of the tomograms and were observed under an optical microscope.

295 As a result, Type A structure, which appeared circular in tomograms, also appeared
296 circular in the corresponding optical microscopic images (Fig. 4a). And Type B structure,
297 which appeared linear in tomograms, appeared flat in the corresponding optical images (Fig.
298 4b). On the other hand, interestingly, Type C, which appeared as void spaces in tomograms,
299 actually appeared flat similarly to Type B in the corresponding microscopic images (Fig. 4c).
300 This means that Type C is actually the same as Type B. These observations raised questions
301 why the filamentous structure take the form of circular or flat and why the void space, which
302 appeared as Type C, was formed.
303
304 **Observation of specimens embedded in LR White resin by X-ray micro-CT and under**
305 **electron microscope**
306 To answer the questions mentioned above, X-ray micro-CT was performed to reconstruct
307 volumes using specimens embedded in LR White resin and tomograms were observed. As a
308 result, however, only Type A was found while Type B and C were not (Fig. 5a). From this
309 observation, we concluded that Type B and C are artifacts formed during paraffin embedding,
310 which is probably due to a problem of infiltration of paraffin into the cell. Therefore, possible
311 causes of formation of Type B and C are suggested as follows: a cell without infiltrated
312 paraffin collapsed before paraffin solidification in the case of Type B, or collapsed after
313 volatilization of xylene from the cell in the case of Type C. Although the flat structure is
314 considered to remain adjacent to the void space in the case of Type C, an artifactual strong
315 halo generated due to tomographic reconstruction around a void space in a tomogram might
316 have made the structure hardly visible.
317 Ultrathin cross-sections were cut from specimens embedded in LR White resin
318 using the ultramicrotome from the same specimens at the corresponding positions of the
319 tomograms. The ultrathin sections were observed under the transmission electron microscope

320 (Fig. 5b, c). A magnified ultrastructural view clearly shows a cellular structure with
321 organelles (plastids) surrounded by the cell wall (Fig. 5c), confirming that the filamentous
322 structure is the rhizoid. White contours and darkly-stained contours of the circular structure
323 (Type A) (Fig. 4a) were revealed to be the cell walls of the rhizoid (Fig. 5c, arrowhead).
324 Quantitative measurements showed that the rhizoids having the diameter of 21.3 ±
325 0.6 (μm, mean ± SE, n = 9) or the thickness of 5.2 ± 0.3 (μm, mean ± SE, n = 8) in the case of
326 circular ones or flattened ones, respectively, were visualized by X-ray micro-CT, which were
327 quantified using tomograms of Ground 10 × *g*_1 specimen.
328
329 **Segmentation and 3D modeling of the rhizoids**
330 Manual segmentation of cross-sectional areas of rhizoids was tried at first to see distribution
331 of rhizoids in a tomographic slice (Fig. 6). Because rhizoids were abundantly observed, it was
332 unrealistic to perform segmentation of all rhizoids manually for every slice through the
333 reconstructed volume. Therefore, we tested two methods of automatic segmentation of cross-
334 sectional areas of rhizoids to label the three types of the rhizoid all together: one is based on
335 contour extraction using Canny edge detector (Fig. 2a) and the other is based on machine
336 learning using TWS 3D (Fig. 2b).
337 As a result, manually-segmented cross-sectional areas of rhizoids appeared in the
338 form of the three types (Type A, B, and C) in tomograms (Fig. 7a, b). Rhizoids are also
339 segmented by either automatic method successfully (Fig. 7c, d). However, cross-sectional
340 areas of rhizoids segmented automatically using TWS 3D (Fig. 7d) appeared slightly larger
341 than the manually-segmented ones (i.e., the ground truth) (Fig. 7b).
342 Automatically-segmented rhizoid areas by the two methods, including all of the
343 three types (Type A, B, and C), were compared with manually-segmented ones. Pixels in
344 automatically-segmented rhizoid areas were categorized into either of the following four

345 groups, true positive, false positive, false negative, or true negative, and a confusion matrix
346 was constructed by summarizing number of pixels in tomograms (Table 1). The confusion
347 matrix actually showed that the number of false positive pixels is about three times larger in
348 the result of the TWS 3D method than that of the Canny edge detector method while the
349 number of false negative pixels in the result of the former is about half as large as that in the
350 result of the latter.

351 The two automatic segmentation methods were evaluated by calculation of
352 accuracy, F1 score, and IoU (Fig. 8). The rhizoid area included all of the three types (Type A,
353 B, and C). As a result, although no significant difference was found between the two
354 automatic segmentation methods for accuracy, measures for performance evaluation such as
355 F1 score and IoU are significantly higher in the result of the TWS 3D method than the Canny
356 edge detection method. Because the area covered by the rhizoids are much smaller than the
357 background, F1 score and IoU are important in the present case. Therefore, the method using
358 TWS 3D was adopted for further analysis.

359

360 **Three-dimensional architecture of the rhizoid system**

361 Three-dimensional isosurface models of the rhizoids were made from
362 automatically-segmented rhizoid areas obtained by application of the TWS 3D method (Fig.
363 9a, b). Distribution density of rhizoids appears to decrease with distance from the base of the
364 rhizoid system (Fig. 9a). To see the distribution of the rhizoids clearly in 3D, the isosurface
365 models were skeletonized (Fig. 9e). A lower magnification view shows a quite dense
366 distribution of the rhizoids in 3D near the base (Fig. 9f). In contrast with this successful
367 observation, we also notified that magnified views of the skeletonized models show problems,
368 such as, artificial excess connections of rhizoids forming of a loop-like structure (Fig. 9c) and
369 artificial interruptions of a rhizoid (Fig. 9d).

Discussion

To capture 3D morphology of the rhizoid system upto centimeter-order depth, specimens were processed for paraffin embedment as the first choice considering its versatility as well as processability: ease of trimming of centimeter-size block. On top of that, we have successfully found that automatic segmentation of rhizoid area based on machine learning (TWS 3D) method enabled to label the rhizoids, which appeared in different three form types in tomograms. In contrast, unfortunately, we had not noticed possible artifacts of paraffin embedment during preparation of Space Moss experiment performing optical microscopy of deparaffinized sections. Therefore, the rhizoid system specimens of Space Moss experiment prepared for X-ray micro-CT were embedded in paraffin and we have to use them for further analyses due to little opportunity for the next space experiment. It is also necessary to solve following problems, including the artifacts caused during paraffin embedment, for the future experiments.

Technical problems regarding embedment of the rhizoid system

As far as the rhizoids become flat and/or void spaces are generated, quantitative analysis of the volume of the rhizoids is not possible because its volume would be underestimated when the rhizoids are flat and overestimated when they are replaced to void spaces.

The artifacts possibly due to paraffin embedment of samples, i.e., flattening of the rhizoids and generation of a void space at the location of the rhizoid, were noticed during 3D observations by X-ray micro-CT while these were not during preparatory observation of paraffin section before performing X-ray micro-CT. Our unawareness of this problem was possibly because the rhizoid tended to be flat after deparaffinization of the paraffin sections

395 because the rhizoids frequently ran obliquely in the section. The reason why the rhizoid cell
396 walls appeared thicker in the paraffin sections is also the same.
397 Flattening of the rhizoids occurred during paraffin embedment is possibly due to
398 difficulty of infiltration of paraffin into the rhizoid cells. We have tested stirring and
399 increasing of substitution steps (%) of paraffin during paraffin infiltration though it is still
400 preliminary. However, these trials were not successful in avoiding of the artifact of rhizoid
401 flattening. Using vacuum oven during paraffin infiltration might help to avoid the artifact of
402 void space formation. On the other hand, embedment of the whole rhizoid systems in LR
403 White resin is highly worth testing to avoid these artifacts.
404
405 **Issues regarding automatic segmentation**
406 TWS 3D provides supervised machine-learning algorithms and thus prediction results may
407 vary depending on the number of epochs (frequency of learning), accuracy for data
408 annotation, and differences in preprocessing of the images. Optimizing these factors will
409 increase accuracy of prediction, which remains to be an issue in the future.
410 The artifacts that became apparent after skeletonization are the artificial excess
411 connection of the rhizoid (Fig. 9c) and the artificial interruption of the rhizoid (Fig. 9d). The
412 former is considered to be due to excessive dilation and the latter is to excessive erosion for of
413 the rhizoid area when Closing (3D) plugin software was applied. These problems may have
414 particularly occurred where densities of the rhizoids are high at, such as, near the base of the
415 gametophore. These are conflicting problems but need to be solved. Providing that current
416 problems regarding artificial excess connection and artificial interruption of the rhizoids are
417 minimized before skeletonization, the length of the rhizoids can be quantitatively analyzed
418 more precisely.
419 Nevertheless, machine learning-based skeletonized 3D model revealed quite dense

distribution of rhizoids near the base (Fig. 9f), and distribution density of rhizoids appears to decrease with distance from the base of the rhizoid system (Fig. 9a). While an overview of the entire architecture shows positive orthogravitropic response (i.e., growth oriented along the gravity vector) of the rhizoid system as a whole (Fig. 9a), it is also noticed that many rhizoids actually show plagiogravitropic responses (i.e., growth oriented obliquely relative to the gravity vector) in a magnified view (Fig. 9e). This is somehow similar to the root system architecture in vascular plants where a combination of orthogravitropism and plagiogravitropism of individual roots results in their wide distribution as a whole.

Conclusions

The rhizoids of *P. patens* having the diameter of 21.3 μm on the average were visualized by refraction-contrast X-ray micro-CT using coherent X-ray optics available at the beamline of the synchrotron radiation facility SPring-8. Filamentous structures which appeared in different three form types in tomograms reconstructed from specimens embedded in paraffin were confirmed to be the rhizoids by optical and electron microscopy. Comprehensive automatic segmentation of the rhizoids, which appeared in different three form types in tomograms, was tested by image processing of contour extraction using Canny edge detector or that based on machine learning. Performance of the automatic segmentation methods was evaluated by comparing with the ground truth images using measures such as F1 score and IoU, revealing that the automatic segmentation method based on machine learning (TWS 3D) is more effective than that using Canny edge detector. Isosurface and skeletonized models of the rhizoid system automatically segmented using machine learning were visualized. This is the first time to successfully visualize the moss rhizoid system in 3D.

Acknowledgements

The synchrotron radiation experiments were performed at the BL20B2 of SPring-8, with the approval of the JASRI (Proposal Nos. 2020A1264 and 2021B1316).

Funding

This work was fully supported by 2020 and 2021 Front loading research grant funded by Japan Aerospace Exploration Agency (JAXA) and Institute of Space and Astronautical Science (ISAS) Expert Committee for Space Environment Utilization Science and partly supported by the “Kibo” utilization feasibility study of JAXA (Japan Aerospace Exploration Agency) and partly supported by JSPS KAKENHI Grant Number JP21K19272.

References

1. O'toole J C and Bland W L (1987) Genotypic variation in crop plant root systems. *Adv. Agron.* 41: 91-145.
2. Jones V A S and Dolan L (2012) The evolution of root hairs and rhizoids. *Ann. Bot. (Lond.)* 110: 205-212.
3. Jang G, Yi K, Pires N D, Menand B and Dolan L (2011) RSL genes are sufficient for rhizoid system development in early diverging land plants. *Development* 138: 2273-2281.
4. Zhang Y, Xiao G, Wang X, Zhang X and Friml J (2019) Evolution of fast root gravitropism in seed plants. *Nat. Commun.* 10: 1-10.
5. Takemura K, Watanabe R, Kameishi R, Sakaguchi N, Kamachi H, Kume A, Fujita T, Karahara I and Hanba Y T (2017) Hypergravity of 10g changes plant growth, anatomy, chloroplast size, and photosynthesis in the moss *Physcomitrella patens*. *Microgravity Sci. Technol.* 29: 467-473.
6. Takemura K, Kamachi H, Kume A, Fujita T, Karahara I and Hanba Y T (2017) A

470 hypergravity environment increases chloroplast size, photosynthesis, and plant growth in
471 the moss Physcomitrella patens. *J. Plant Res.* 130: 181-192.
472 7. Flavel R J, Guppy C N, Tighe M, Watt M, Mcneill A and Young I M (2012) Non-
473 destructive quantification of cereal roots in soil using high-resolution X-ray tomography.
474 *J. Exp. Bot.* 63: 2503-2511.
475 8. Mairhofer S, Zappala S, Tracy S, Sturrock C, Bennett M J, Mooney S J and Pridmore T P
476 (2013) Recovering complete plant root system architectures from soil via X-ray μ-
477 computed tomography. *Plant Methods* 9: 1-7.
478 9. Rogers E D, Monaenkova D, Mijar M, Nori A, Goldman D I and Benfey P N (2016) X-
479 ray computed tomography reveals the response of root system architecture to soil texture.
480 *Plant Physiol.* 171: 2028-2040.
481 10. Daly K R, Tracy S R, Crout N M J, Mairhofer S, Pridmore T P, Mooney S J and Roose T
482 (2018) Quantification of root water uptake in soil using X-ray computed tomography and
483 image-based modelling. *Plant Cell Environ.* 41: 121-133.
484 11. Gao W, Schlüter S, Blaser S R G A, Shen J and Vetterlein D (2019) A shape-based
485 method for automatic and rapid segmentation of roots in soil from X-ray computed
486 tomography images: Rootine. *Plant Soil* 441: 643-655.
487 12. Yoshida Y, Arita T, Otani J and Sawa S (2020) Visualization of Toyoura sand-grown
488 plant roots by X-ray computer tomography. *Plant Biotechnol.* 37: 481-484.
489 13. Teramoto S, Takayasu S, Kitomi Y, Arai-Sanoh Y, Tanabata T and Uga Y (2020) High-
490 throughput three-dimensional visualization of root system architecture of rice using X-ray
491 computed tomography. *Plant Methods* 16: 1-14.
492 14. Kurogane T, Tamaoki D, Yano S, Tanigaki F, Shimazu T, Kasahara H, Yamauchi D,
493 Uesugi K, Hoshino M, Kamisaka S, Mineyuki Y and Karahara I (2021) Visualization of
494 Arabidopsis root system architecture in 3D by refraction-contrast X-ray micro-computed

tomography. *Microscopy* 70: 536–544.

15. Kume A, Kamachi H, Onoda Y, Hanba Y T, Hiwatashi Y, Karahara I and Fujita T (2021) How plants grow under gravity conditions besides 1 *g*: perspectives from hypergravity and space experiments that employ bryophytes as a model organism. *Plant Mol. Biol.* 107: 279–291.
16. Nishiyama T, Hiwatashi Y, Sakakibara K, Kato M and Hasebe M (2000) Tagged Mutagenesis and Gene-trap in the Moss, Physcomitrella patens by Shuttle Mutagenesis. *DNA Research* 7: 9-17.
17. Karahara I, Suto T, Yamaguchi T, Yashiro U, Tamaoki D, Okamoto E, Yano S, Tanigaki F, Shimazu T, Kasahara H, Kasahara H, Yamada M, Hoson T, Soga K and Kamisaka S (2020) Vegetative and reproductive growth of Arabidopsis under microgravity conditions in space. *J. Plant Res.* 133: 571–585.
18. Ishioka N, Suzuki H, Asashima M, Kamisaka S, Mogami Y, Ochiai T, Aizawa-Yano S, Higashibata A, Ando N, Nagase M, Ogawa S, Shimazu T, Fukui K and Fujimoto N (2004) Development and verification of hardware for life science experiments in the Japanese Experiment Module "Kibo" on the International Space Station. *J. Gravit. Physiol.* 11: 81-91.
19. Yano S, Kasahara H, Masuda D, Tanigaki F, Shimazu T, Suzuki H, Karahara I, Soga K, Hoson T, Tayama I, Tsuchiya Y and Kamisaka S (2013) Improvements in and actual performance of the Plant Experiment Unit onboard Kibo, the Japanese experiment module on the international space station. *Adv. Space Res.* 51: 780-788.
20. Karahara I, Umemura K, Soga Y, Akai Y, Bando T, Ito Y, Tamaoki D, Uesugi K, Abe J, Yamauchi D and Mineyuki Y (2012) Demonstration of osmotically dependent promotion of aerenchyma formation at different levels in the primary roots of rice using a "sandwich" method and X-ray computed tomography. *Ann. Bot. (Lond.)* 110: 503-509.

520 21. Kremer J R, Mastronarde D N and Mcintosh J R (1996) Computer visualization of three-
521 dimensional image data using IMOD. *J. Struct. Biol.* 116: 71-76.
522 22. Karahara I, Suda J, Tahara H, Yokota E, Shimmen T, Misaki K, Yonemura S, Staehelin L
523 A and Mineyuki Y (2009) The preprophase band is a localized center of clathrin-
524 mediated endocytosis in late prophase cells of the onion cotyledon epidermis. *Plant J.* 57:
525 819-831.
526 23. Canny J (1986) A computational approach to edge detection. *IEEE Trans. Pattern Anal.*
527 *Mach. Intell.* PAMI-8: 679-698.
528 24. Schindelin J, Arganda-Carreras I, Frise E, Kaynig V, Longair M, Pietzsch T, Preibisch S,
529 Rueden C, Saalfeld S, Schmid B, Tinevez J-Y, White D J, Hartenstein V, Eliceiri K,
530 Tomancak P and Cardona A (2012) Fiji: an open-source platform for biological-image
531 analysis. *Nat. Meth.* 9: 676-682.
532 25. Gibara T (2013) Canny Edge Detector.
533 https://imagej.nih.gov/ij/plugins/canny/index.html. Accessed Apr. 21 2022.
534 26. Legland D, Arganda-Carreras I and Andrey P (2016) MorphoLibJ: integrated library and
535 plugins for mathematical morphology with ImageJ. *Bioinformatics* 32: 3532-3534.
536 27. Arganda-Carreras I, Kaynig V, Rueden C, Eliceiri K W, Schindelin J, Cardona A and
537 Sebastian Seung H (2017) Trainable Weka Segmentation: a machine learning tool for
538 microscopy pixel classification. *Bioinformatics* 33: 2424-2426.
539 28. Frank E, Hall M A and Witten I H (2016) The WEKA workbench. online appendix. In:
540 *Data mining: Practical machine learning tools and techniques, Fourth Edition*, eds.
541 Witten I H, Frank E, Hall M A and Pal C J, (Morgan Kaufmann Publishers).
542
543
544 **Figure legends**

Fig. 1. Specimen preparation and X-ray micro-CT scanning. (a, b) Lateral views of gametophores and rhizoids of *P. patens* grown on/in agar media observed under a dissecting microscope before (a) and after (b) embedding in paraffin. Specimen example: Ground 1 × *g*_SN17. Scale bars = 10 mm. (c) Experimental set up at the beamline BL20B2. Arrows indicate the X-ray path. Rhizoid system embedded in paraffin was placed on a rotation stage. A seed of morning glory was placed on the paraffin block as a position marker.

Fig. 2. Workflow for automatic segmentation of cross-sectional areas of rhizoids. (a) A method based on contour extraction using Canny edge detector. (b) A method based on machine learning using TWS 3D. Specimen example: Ground 1 × *g*_82.

Fig. 3. Observation of the reconstructed volume of the rhizoid system of *P. patens* embedded in paraffin. Cross sections of the three types of filamentous structures observed in the tomographic slices (a-c). (a) Type A, (b) Type B, and (c) Type C structures. (d) Overview of a cross-sectional tomogram. Specimen example: a-c, Ground 1 × *g*_27; d, Space 1 × *g*_003. Scale bars = 50 μm (a-c), 1 mm (d).

Fig. 4. Comparison of tomographic images and optical microscopic images of the three types of the filamentous structures observed in the rhizoid system of *P. patens* embedded in paraffin. (a) Type A, (b) Type B, and (c) Type C structures. The upper row, CT: tomographic images. The lower row, OM: optical microscopic images of paraffin sections obtained at the position corresponding to its tomographic images. Specimen example: Ground 10 × *g*_1, 2. Scale bars = 50 μm.

570 **Fig. 5.** Comparison of a tomographic image and electron microscopic images of Type A
571 structure observed in the rhizoid system of *P. patens* embedded in LR White resin. (a) A
572 tomographic image, where three Type A structures are visible (arrowheads). (b) An electron
573 microscopic image obtained at the position corresponding to the tomographic image of (a),
574 where the same three structures are visible (arrowheads). (c) A magnified electron
575 microscopic image of Type A structure, i.e., cross-sectional view of a rhizoid cell. An
576 arrowhead shows cell wall. Specimen examples: Space 1 × *g*_B003 (a, b), Space 1 × *g*_004
577 (c). Scale bars = 20 μm (a, b), 5 μm (c).
578
579 **Fig. 6.** An overview of the rhizoid distribution in a cross-sectional tomographic slice of the
580 rhizoid system of *P. patens* embedded in paraffin. Cross sectional areas of rhizoids are
581 manually labelled in red. Specimen example: Ground 1 × *g*_27. Scale bar = 1 mm.
582
583 **Fig. 7.** Comparison of manual and automatic segmentation of cross-sectional areas of rhizoids
584 that appeared in the form of the three types in tomograms. (a) Original tomogram. (b) Manual
585 segmentation (ground truth). (c) Automatic segmentation based on contour extraction using
586 Canny edge detector. (d) Automatic segmentation based on machine learning using TWS 3D.
587 Rounded squares indicate Type A (blue), Type B (green), and Type C (red). Specimen
588 example: Ground 1 × *g*_27.
589
590 **Fig. 8.** Comparison of accuracy (a), F1 score (b), and IoU (c) values between the automatic
591 segmentation method based on contour extraction using Canny edge detector and the one
592 based on machine learning using TWS 3D. N. S., Not significant ($P \geq 0.05$); *, $P < 0.05$
593 (Welch's *t*-test). n = 36.
594

Fig. 9. Three-dimensional models of the rhizoid system of *P. patens* embedded in paraffin. Isosurface models of the rhizoids (a, entire view; b, magnified view). Skeletonized individual rhizoid models (e). Magnified views of the skeletonized rhizoid models showing artificial formation of a loop-like structure (c) and artificial interruptions (d). A lower magnification view of skeletonized rhizoid models showing a part near the base of the rhizoid system (f). Models were visualized using 3D viewer of ImageJ software (a) or Imod software (b-f). Specimen example: Ground 1 × g_27 (a), Ground 1 × *g*_82 (b-f). Scale bars = 1000 μm (a, f), 50 μm (b, c, d), 500 μm (e).

Supplementary Fig. 1. Movie made from consecutive CT tomographic slices in z direction. Yellow rectangular shows a filamentous structure which changes its form Type A, C, A, to B consecutively. Specimen example: Ground 10 × *g*_2. Scale bar = 50 μm.

Supplementary Fig. 2. Evaluation of the automatic segmentation methods**.** Rhizoid (white) and background (black) areas obtained by manual segmentation (ground truth) (a) and automatic segmentation (b) were compared and categorized into the areas of four groups: true positive (orange, TP), false positive (blue, FP), false negative (green, FN), and true negative (gray, TN) (c). A confusion matrix was constructed by counting the number of pixels in each categorized area (d). (e) Formulas calculating accuracy, F1 score, and Intersection over Union (IoU).

Table 1. Confusion matrix results for evaluating two automatic segmentation methods. Numbers are summary of pixel numbers counted on 9 different areas of 256 × 256 pixels sampled from 4 tomograms of the specimens of Ground 1 × *g*_27, 82, Space 1 × *g*_004, and

Space μ × *g*_102.

		Confusion matrix classification		Canny edge detection		TWS 3D	
		Predicted image		Predicted image		Predicted image	
		Rhizoid	Back-ground	Rhizoid	Back-ground	Rhizoid	Back-ground
Actual (Ground Truth) image	Rhizoid	True Positive	False Negative	39053	30636	53472	16217
	Back-ground	False Positive	True Negative	17020	2272587	59298	2230309

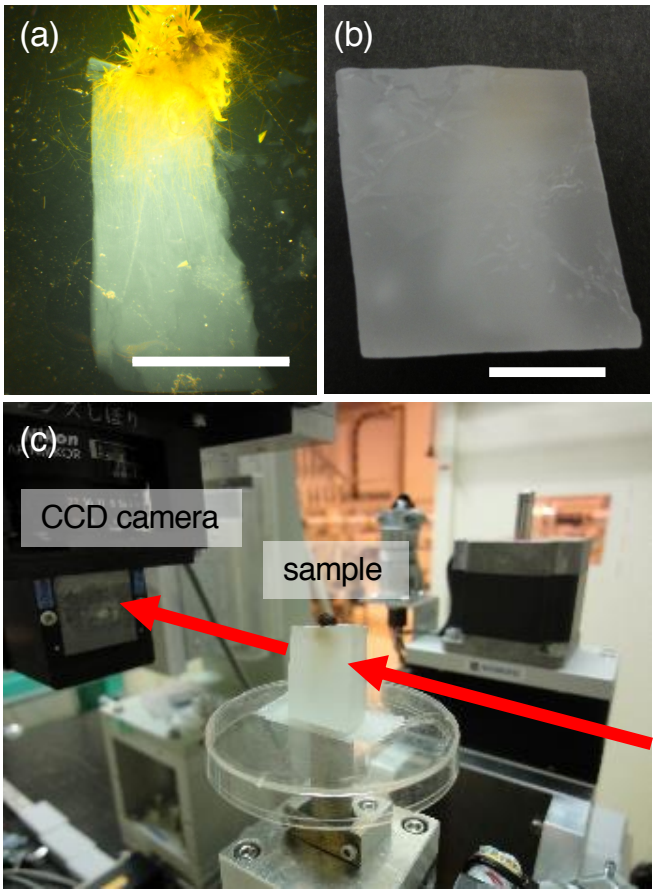

Fig. 1. Specimen preparation and X-ray micro-CT scanning. (a, b) Lateral views of gametophores and rhizoids grown on/in agar media observed under a dissecting microscope before (a) and after (b) embedding in paraffin. Specimen example: Ground 1 × *g*_SN17. Scale bars = 10 mm. (c) Experimental set up at the beamline BL20B2. Arrows indicate the X-ray path. Rhizoid system embedded in paraffin was placed on a rotation stage. A seed of morning glory was placed on the paraffin block as a position marker.

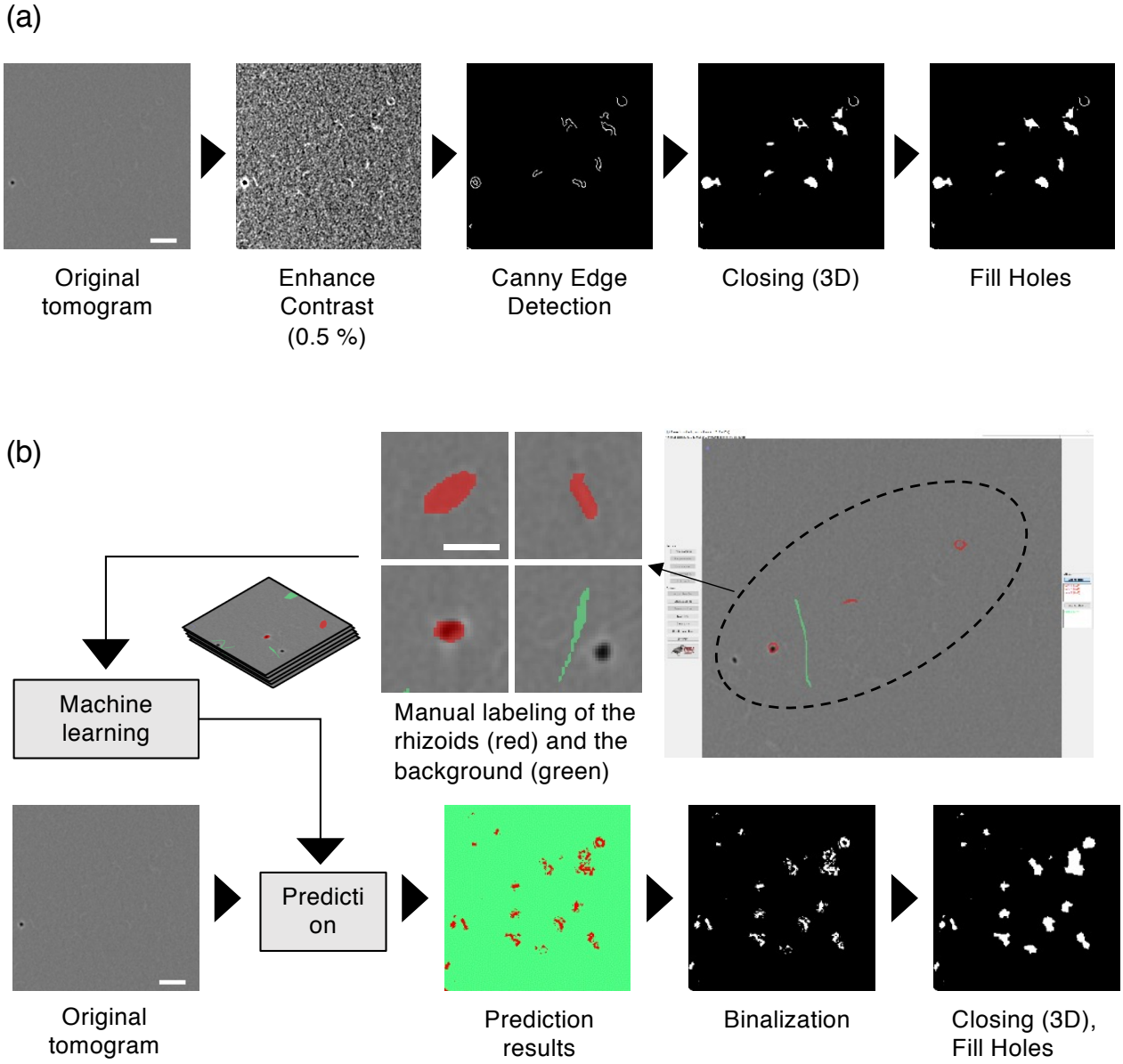

Fig. 2. Workflow for automatic segmentation of cross-sectional areas of rhizoids. (a) A method based on contour extraction using Canny edge detection. (b) A method based on machine learning using TWS 3D. Specimen example: Ground 1 × *g*_82.

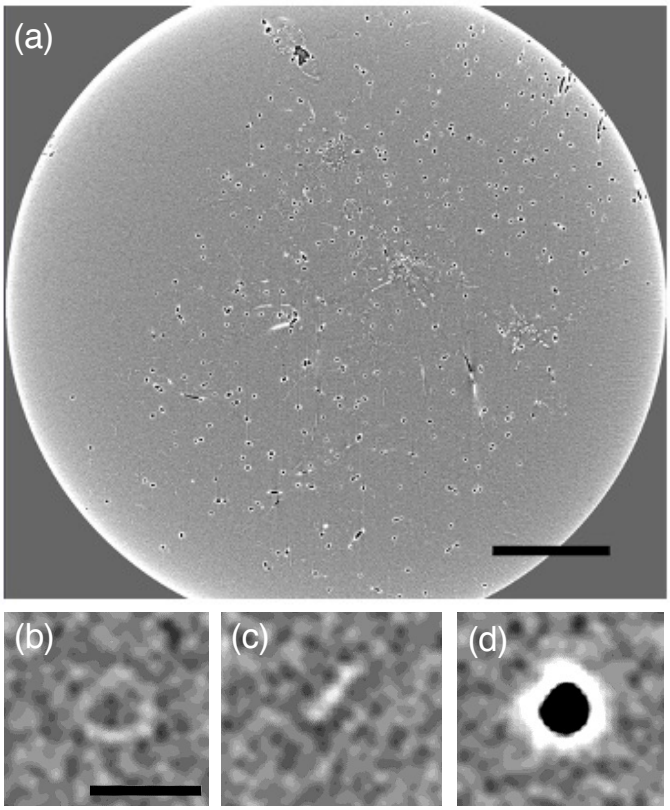

Fig. 3. Observation of the reconstructed volume of the rhizoid system of *P. patens* embedded in paraffin. Cross sections of the three types of filamentous structures observed in the tomographic slices (a-c). (a) Type A, (b) Type B, and (c) Type C structures. (d) The entire view of a cross-sectional tomogram. Specimen example: a-c, Ground 1 × *g*_27; d, Space 1 × *g*_003. Scale bars = 50 µm (a-c), 1 mm (d).

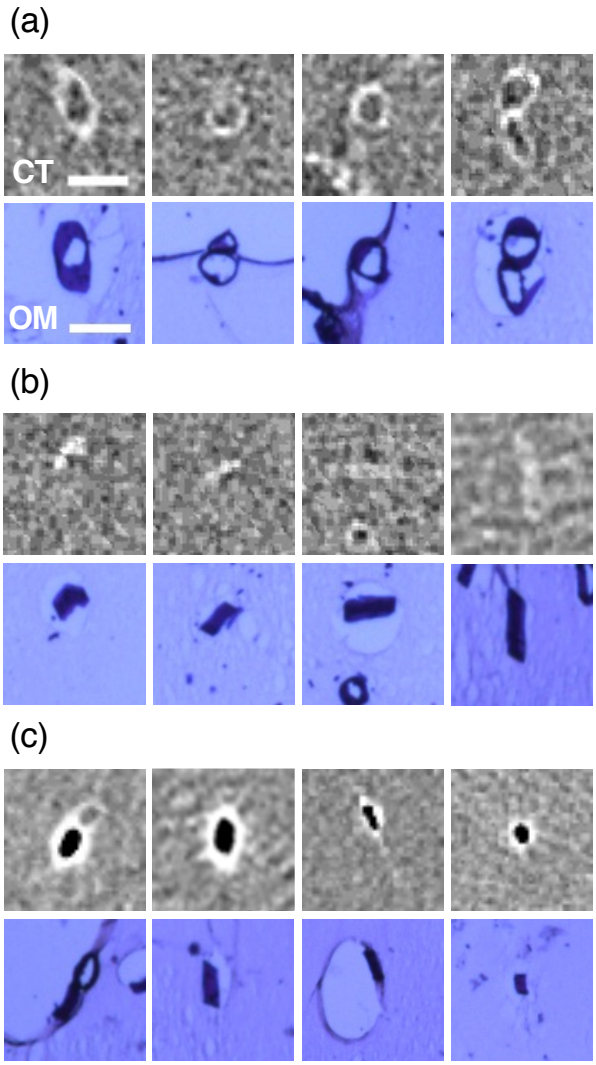

Fig. 4. Comparison of tomographic images and optical microscopic images of the three types of the filamentous structures observed in the rhizoid system of *P. patens* embedded in paraffin. (a) Type A, (b) Type B, and (c) Type C structures. The upper row, CT: tomographic images. The lower row, OM: optical microscopic images of paraffin sections obtained at the position corresponding to its tomographic images. Specimen example: Ground 10 × *g*_1, 2. Scale bars = 50 µm.

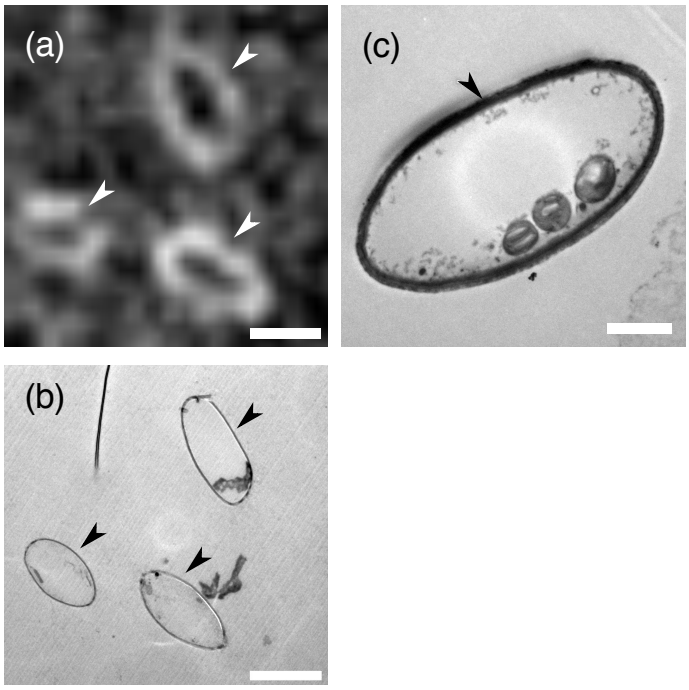

Fig. 5. Comparison of a tomographic image and electron microscopic images of Type A structure observed in the rhizoid system of *P. patens* embedded in LR White resin. (a) A tomographic image, where three Type A structures are visible (arrowheads). (b) An electron microscopic image obtained at the position corresponding to the tomographic image of (a), where the same three structures are visible (arrowheads). (c) A magnified electron microscopic image of Type A structure, i.e., cross-sectional view of a rhizoid cell. An arrowhead shows cell wall. Specimen examples: Space 1 × *g*_B003 (a, b), Space 1 × *g*_004 (c). Scale bars = 20 µm (a, b), 5 µm (c).

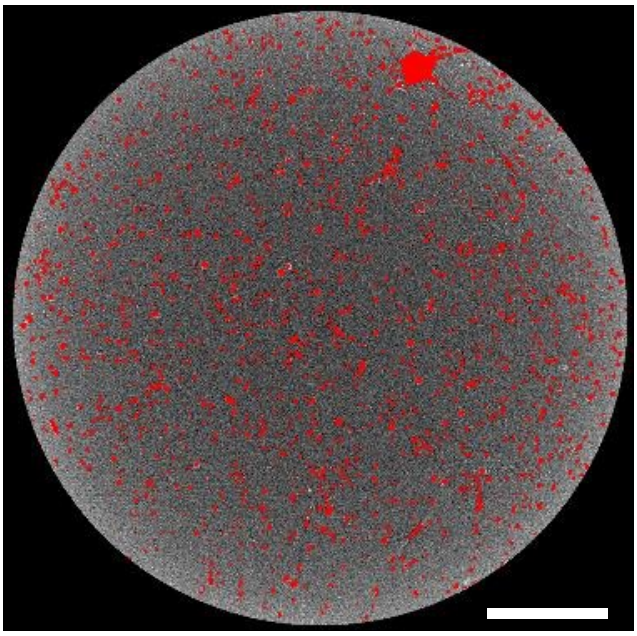

Fig. 6. An overview of the rhizoid distribution in a cross-sectional tomographic slice of the rhizoid system of *P. patens* embedded in paraffin. Cross sectional areas of rhizoids are manually labelled in red. Specimen example: Ground 1 × *g*_27. Scale bar = 1 mm.

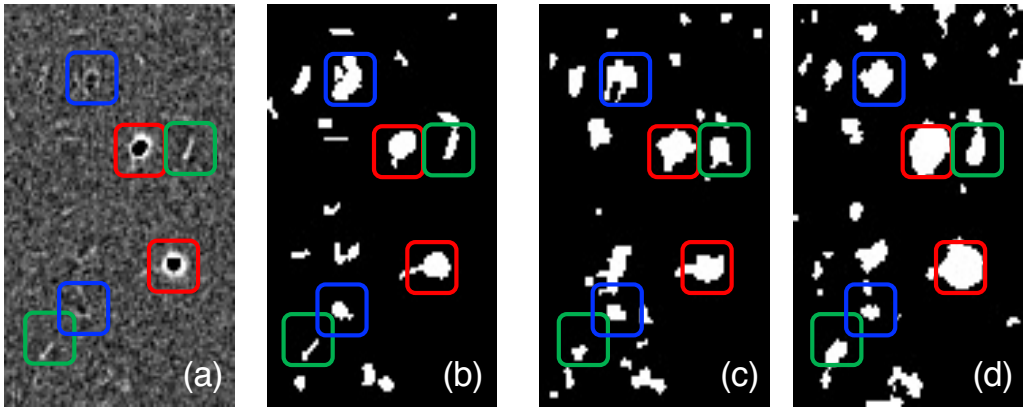

Original tomogram | Manual segmentation (ground truth) | Automatic segmentation (Canny edge detection) | Automatic segmentation (TWS 3D)

Fig. 7. Comparison of manual and automatic segmentation of cross-sectional areas of rhizoids that appeared in the form of the three types in tomograms. (a) Original tomogram. (b) Manual segmentation (ground truth). (c) Automatic segmentation based on contour extraction using Canny edge detection. (d) Automatic segmentation based on machine learning using TWS 3D. Rounded squares indicate Type A (blue), Type B (green), and Type C (red). Specimen example: Ground 1 × *g*_27.

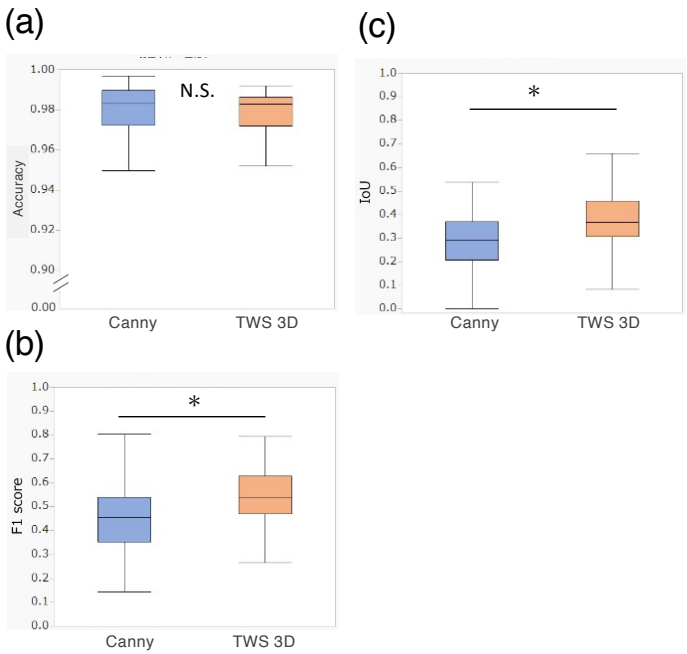

Fig. 8. Comparison of accuracy (a), F1 score (b), and IoU (c) values between the automatic segmentation method based on contour extraction using Canny edge detection and the one based on machine learning using TWS 3D. N. S., Not significant ($P \geq 0.05$); *, $P < 0.05$ (Welch's *t*-test). n = 36.

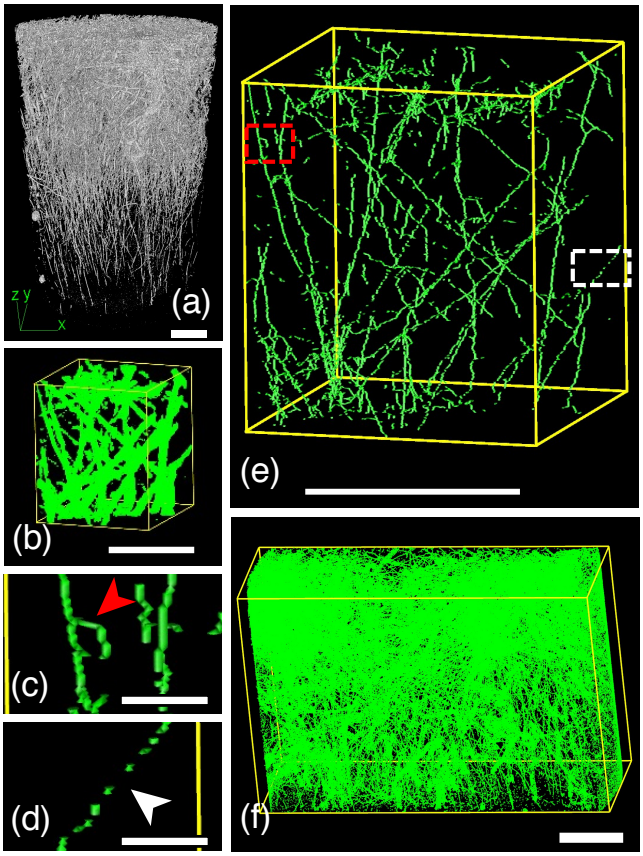

Fig. 9. Three-dimensional models of the rhizoid system of P. patens embedded in paraffin. Isosurface models of the rhizoids (a, entire view; b, magnified view). Skeletonized individual rhizoid models (e). Magnified views of the skeletonized rhizoid models showing artificial formation of a loop-like structure (c) and artificial interruptions (d). A lower magnification view of skeletonized rhizoid models showing a part near the base of the rhizoid system (f). Models were visualized using 3D viewer of ImageJ software (a) or Imod software (b-f). Specimen example: Ground 1 × g_27 (a), Ground 1 × g_82 (b-f). Scale bars = 1000 µm (a, f), 50 µm (b, c, d), 500 µm (e).